

Interplay between intercalated oxygen superstructures and monolayer *h*-BN on Cu(100)

Chuanxu Ma,¹ Jewook Park,¹ Lei Liu,² Yong-Sung Kim,^{1,2,3,4} Mina Yoon,^{1,2} Arthur P. Baddorf,¹ Gong Gu,² and An-Ping Li^{1,*}

¹Center for Nanophase Materials Sciences, Oak Ridge National Laboratory, Oak Ridge, Tennessee 37831, USA

²The University of Tennessee, Knoxville, Tennessee 37996, USA

³Korea Research Institute of Standards and Science, Yuseong, Daejeon 305-340, Korea

⁴Department of Nano Science, Korea University of Science and Technology, Daejeon 305-350, Korea

(Received 12 April 2016; revised manuscript received 17 June 2016; published 18 August 2016)

The confinement effect of intercalated atoms in van der Waals heterostructures can lead to interesting interactions between the confined atoms or molecules and the overlaying two-dimensional (2D) materials. Here we report the formation of ordered Cu(100) $p(2 \times 2)$ oxygen superstructures by oxygen intercalation under the monolayer hexagonal boron nitride (*h*-BN) on Cu after annealing. By using scanning tunneling microscopy and x-ray photoelectron spectroscopy, we identify the superstructure and reveal its roles in passivating the exposed Cu surfaces, decoupling *h*-BN and Cu, and disintegrating *h*-BN monolayers. The oxygen superstructure appears as a 2D pattern on the exposed Cu surface or quasi-1D stripes of paired oxygen intercalated in the interface of *h*-BN and Cu predominantly oriented along the moiré modulations. The oxygen superstructure is shown to etch the overlaying *h*-BN monolayer in a thermal annealing process. After extended annealing, the *h*-BN monolayer disintegrates into nanoislands with zigzag edges. We discuss the implications of these findings on the stability and oxidation resistance of *h*-BN and relate them to challenges in process integration and 2D heterostructures.

DOI: [10.1103/PhysRevB.94.064106](https://doi.org/10.1103/PhysRevB.94.064106)

I. INTRODUCTION

Interfaces provide spatial confinement that can enable interesting properties that would not exist in the constituent materials alone, such as two-dimensional (2D) electron gas [1,2], heterogeneous catalysis [3], and novel dynamics of atoms or molecules [4,5]. The atomically sharp interface between a weakly coupled 2D material and its substrate generates a unique 2D space for exploring the molecule-substrate interactions and surface reactivity [6–8]. In particular, the intercalation of atoms and molecules in the interface is a promising route to modify the structures and electronic properties of 2D materials [9,10]. As the thinnest insulating 2D material, the monolayer hexagonal boron nitride (*h*-BN), which can be grown by chemical vapor deposition (CVD) directly on transition metal substrates [11–13], is a good overlayer for studying interfacial interactions. Oxygen is shown to intercalate the interface of *h*-BN and metal substrate [14], which can mediate the catalytic etching of *h*-BN [15–17]. However, the structure of the intercalated oxygen involved in the etching process remains unclear. Moreover, the monolayer *h*-BN made of strong covalent bonds, exhibits profound mechanical, chemical, and temperature stability [18–22], and promises a wide range of applications as a deep ultraviolet emitter [23], dielectric layer [24], protective coating [25], etc. Recent reports recommend *h*-BN as a strong oxidation resistance barrier for both metal substrates and graphene [26]. On the other hand, theoretical calculations on the oxidation of monolayer *h*-BN suggest that oxygen atoms are first absorbed on top of BN planes to form energetically favorable oxygen chains and then the dissociation of the B–O–N bonds cuts the BN nanosheets along the chains [27,28]. Thus, the stability of *h*-BN as an oxidation barrier and the oxygen etching

process both remain to be evaluated, especially when facing an interface between *h*-BN and a catalytic metal.

In the present work, using scanning tunneling microscopy (STM), we show the formation of an ordered $p(2 \times 2)$ superstructure after annealing the monolayer *h*-BN on a Cu(100) system at 600 °C in ultrahigh vacuum (UHV). X-ray photoelectron spectroscopy (XPS) measurements confirm the superstructure as $p(2 \times 2)$ oxygen, a long sought-after surface configuration of Cu(100) with low oxygen coverage. The oxygen is introduced by intercalation during the sample exposure to air before transferring to UHV. Density functional theory (DFT) calculations suggest an important role of the confinement effect of the monolayer *h*-BN in the formation of the superstructure. The $p(2 \times 2)$ -O superstructure is shown to decouple the monolayer *h*-BN and facilitate its etching process on the Cu(100).

II. EXPERIMENTAL AND COMPUTATIONAL METHODS

Large-scale *h*-BN monolayers were grown by atmospheric-pressure CVD on 25- μ m-thick Cu foils (Alfa Aesar, 46986), as described in recent reports [29,30]. The typical growth time was 30–60 min to obtain nearly full coverage of monolayer *h*-BN on the Cu surface as shown in the Supplemental Material, Fig. S1 [31]. The predominant Cu surface orientation has been found to be (100) [29,32,33]. Before being loaded into the UHV, samples were exposed to air for 1 month (sample A) or 20 h (sample B). Then, the samples were annealed in two different steps in UHV with a background pressure better than 10^{-10} Torr. The first step was annealing at 430 °C overnight (12 h) to clean up the sample surface. The *h*-BN samples were checked by STM for cleanliness and no oxygen superstructures were observed (as shown in the Supplemental Material, Fig. S2 [31]). The second step was annealing at 600 °C to form the superstructures. For the second step we varied the annealing time, 4 and 12 h, respectively, for sample A and 1 h for sample B, in order to examine different stages of

*apli@ornl.gov

the oxygen intercalation and etching process of BN. The STM characterizations were performed at room temperature under UHV conditions. An electrochemical etched and well-cleaned tungsten tip was used. All STM images were acquired with a constant-current mode. The dI/dV spectra were recorded using a lock-in amplifier with a sinusoidal modulation ($f = 1000$ Hz, $V_{\text{mod}} = 40$ mV) by turning off the feedback loop gain. The polarity of the applied voltage refers to the sample bias with respect to the tip.

The DFT calculations were performed as implemented in the Vienna *ab initio* simulation package (VASP) [34,35]. The projector augmented wave (PAW) pseudopotentials [36,37], and the generalized gradient approximation (GGA) parametrized by Perdew, Burke, and Ernzerhof (PBE) [38] for the exchange-correlation energy of electrons were employed, including the DFT-D2 scheme of Grimme for the van der Waals interactions [39,40]. The Cu(100) slab with six Cu layers and $p(4 \times 5n)$ surface periodicity ($n = 1, 2$, and 4 , the corresponding numbers of Cu atoms are 120, 240, and 480, respectively) were used for the host substrate supercell and the PBE-D2 optimized Cu lattice constant of 2.568 Å was used. The two bottom Cu layers were fixed to mimic bulk. The BN 4 units along the zigzag direction were lattice matched with the Cu 4 units with 2% tensile strain, and the BN $3\sqrt{3}$ units along the armchair direction were wrinkled with the Cu 4 unit periodicity with releasing the 1% compressive strain. The $2 \times 4 \times 1$ Γ -centered mesh for the Cu $p(4 \times 5)$ supercell and equivalents for the Cu $p(4 \times 10)$ and $p(4 \times 20)$ supercells were used for the k -point sampling to sum over the Brillouin zone.

III. RESULTS AND DISCUSSION

Figure 1(a) shows a large-scale STM image of the *h*-BN monolayer on Cu (sample A) after air exposure (1 month), overnight degassing (430°C), and annealing at 600°C in UHV for 4 h. The Cu foil used here exhibits exclusive (100) surface orientations after the thermal annealing as part of the *h*-BN growth process [30,32,33]. Two different types of region are observed: reconstructed regions and regions featureless at this resolution. A magnified image of a featureless region is shown in the inset with atomic resolution, with the atomistic model of *h*-BN superimposed. The periodicity and the threefold symmetry of the image are consistent with the *h*-BN structure, with the bright spots corresponding to N atoms at the negative sample biases [32,41–43]. The featureless regions are therefore attributed to the *h*-BN monolayer. Notably, the reconstructed regions are shown as either 2D patches or quasi-1D chains of two paired bright spots [the white dashed box in Fig. 1(a)]. Here the *h*-BN monolayer has been etched away at the reconstructed regions (to be discussed in Fig. 6). The ordered superstructure is more clearly shown in Fig. 1(b), and confirmed by the fast Fourier transform (FFT) image in Fig. 1(c). From the line profile of the FFT patterns in Fig. 1(d), we find a lattice constant of 0.51 ± 0.01 nm. This value is larger than the period of the $c(2 \times 2)$ superstructure on Cu(100) (~ 0.36 nm) [44], but equal to that of the $p(2 \times 2)$ superstructure (~ 0.51 nm) [45]. Therefore, the observed ordered patterns are assigned to a $p(2 \times 2)$ superstructure on Cu(100).

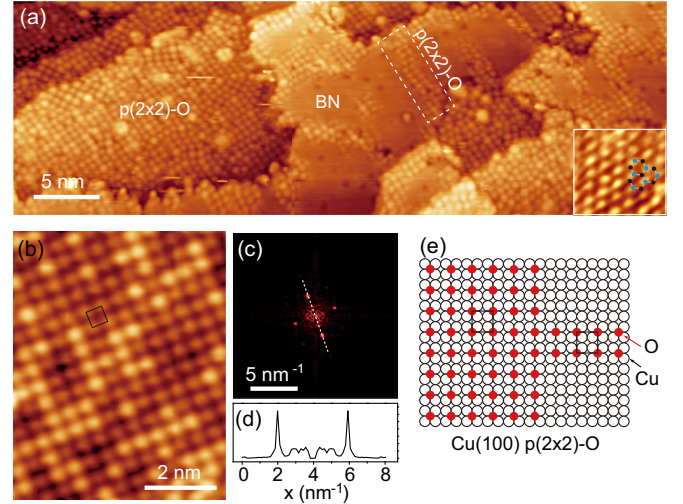


FIG. 1. Structures of *h*-BN/Cu(100) after 600°C annealing (4 h, following overnight degassing at 430°C after 1 month air exposure; sample A). (a) Large-area STM topographic image showing typical reconstructed region and *h*-BN region (-1 V, 100 pA). The dashed box marks a representative quasi-1D ordered superstructure. Inset: Atomically resolved STM image of the monolayer *h*-BN (-1 V, 100 pA) with a structure model superposed (blue: N; black: B). (b) Magnified STM image of reconstructed region, with a rectangle marking the square unit cell (-1 V, 100 pA). (c) Fast Fourier transform (FFT) pattern of (b). (d) Profile along the white dashed line in (c). The lattice constant of the reconstruction, ~ 0.51 nm, is obtained from the FFT. (e) Atomic structure model of the $p(2 \times 2)$ -O superstructure on Cu(100).

To examine the chemical origin of the reconstructed superstructure in the monolayer *h*-BN on Cu, we performed XPS measurements on the same sample A after the STM characterization by transferring to a different UHV chamber through air (exposure < 1 h). Then, the sample was annealed at a low temperature to remove hydrocarbon surface absorbates (see the Supplemental Material, Fig. S3 [31]). XPS core-level spectra were obtained at room temperature by using a SPECS Focus 500 monochromated Al K_α x-ray source and PHOIBOS-150 hemispherical analyzer. Figure 2(a) shows a survey spectrum, where emission peaks associated with Cu, O1s, N1s, and B1s emissions are marked, respectively. Both B1s and N1s core levels are symmetric in Figs. 2(b) and 2(c), with peak positions located at 190.5 and 398.0 eV, respectively, typical for *h*-BN [17,20,26,30,46]. While taking the atomic sensitivity factors into account, the atom ratio N/B is about 1 (see the Supplemental Material, Fig. S3 [31]), supporting *h*-BN compound. Interestingly, there is a strong signal of O1s emission in Fig. 2(d), even after effectively removing surface contaminants. The main component of O1s is located at 530.2 eV, a binding energy indicative of a metal oxide [46]. The peak for O1s also shows a shoulder near 531.6 eV that can be reduced by post ambient exposure annealing (see the Supplemental Material, Fig. S3 [31]) and is attributed to the hydroxide contaminations [46]. The XPS data provide an atom ratio N/O of about 1.4 (only considering the main component of O1s) (see the Supplemental Material, Fig. S3 [31]). The nitrogen in the *h*-BN lattice has an atomic

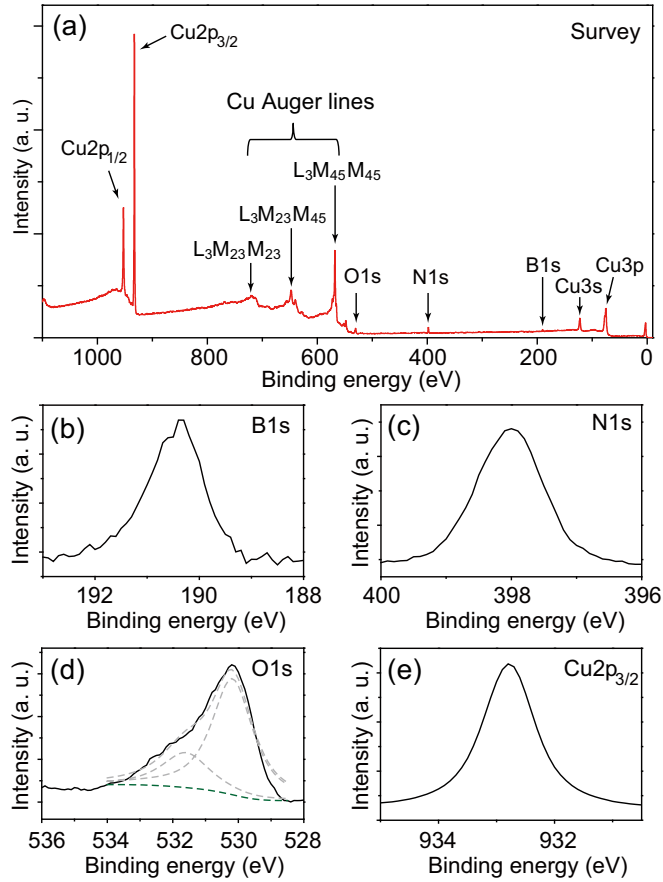


FIG. 2. XPS spectra of monolayer *h*-BN on Cu(100) after annealing at 600 °C in UHV. (a) Survey spectrum, (b) B1s emission spectrum, (c) N1s emission spectrum, (d) O1s emission spectrum, and (e) Cu2p_{3/2} emission spectrum. The O1s spectrum shows two components located at 530.2 and 531.6 eV (dashed lines), respectively.

density of about 18.5 N atoms/nm², while the oxygen in the $p(2 \times 2)$ superstructure has an atomic density of about 3.8 O atoms/nm². If the superstructure is $p(2 \times 2)$ -O, the surface area covered by the superstructure is expected to be about 3.5 times more than the surface area covered by *h*-BN. Indeed, the statistics obtained from STM images indicate an area ratio of $p(2 \times 2)$ and *h*-BN to be about 3.4–3.9.

Our STM and XPS analyses confirm that the superstructures are the oxygen induced $p(2 \times 2)$ reconstruction on Cu(100), a proposed structure model of which is shown in Fig. 1(e). The oxygen atoms at the hollow sites appear as bright spots in STM images [Figs. 1(a) and 1(b)] due to the enhanced occupied density of states near the O atom [47]. Interestingly, although the $p(2 \times 2)$ -O is believed to be the most stable configuration for the adsorption of oxygen on the Cu(100) surface [47] with low oxygen coverage (0.25 monolayer, ML) and was predicted to exist on Cu(100) decades ago [48], so far there does not appear to be any experimental report for such an ordered structure on Cu(100) [47]. The most documented surface configurations for oxygen-adsorbed Cu(100) are $c(2 \times 2)$ and $(2\sqrt{2} \times \sqrt{2}) R45^\circ$ with a higher effective oxygen coverage (both 0.5 ML; O adsorption sites same for the two) [47,49,50]. As explained

below with theoretical calculations, the unique experimental demonstration of the Cu(100) $p(2 \times 2)$ -O superstructure here can be attributed to a confinement effect in the interface between the weakly coupled *h*-BN and Cu.

We further examined another sample (sample B) that had been exposed to air for a shorter period of time (20 h) and then outgassed (430 °C, overnight) and annealed (600 °C, 1 h) in UHV. We identified three characteristic regions: fully reconstructed checkerboardlike $p(2 \times 2)$ -O region (FRR) on Cu with BN layer completely etched away, partially reconstructed region (PRR) consisting of quasi-1D oxygen stripes formed at the empty space between *h*-BN monolayer and Cu, and pristine BN on Cu. The STM image presented in Fig. 3(a) clearly demonstrates the coexistence of these three regions. The apparent heights of different regions are shown in Fig. 3(b), where panels 1–4 correspond to the profiles respectively along lines 1–4 marked in Fig. 3(a). A step of 1.8 Å is seen along line 1, which corresponds to an atomic step on Cu(100) substrate. When an FRR is surrounded by striped regions of PRR and *h*-BN on a same Cu terrace (lines 2 and 3), the PRR is about 2.2 Å higher than FRR, and about 0.7 Å higher than the *h*-BN. The height differences of these regions are further confirmed by examining the profile along line 4, where the PRR is only 0.4 Å higher than the FRR as the former sits on a Cu terrace one atomic step lower than the latter (0.4 + 1.8 = 2.2 Å). Although the STM topography image can only show the apparent height at a particular sample bias, considering the calculated height (~ 0.8 Å) of adsorbed O on Cu(100) [47], this analysis allows us to propose that the FRR is $p(2 \times 2)$ -O without an *h*-BN overlayer [i.e., $p(2 \times 2)$ -O/Cu] and that the PRR is monolayer *h*-BN atop the $p(2 \times 2)$ -O superstructure, namely, there exists an intercalated $p(2 \times 2)$ -O layer between the *h*-BN and the Cu in the PRR [i.e., BN/ $p(2 \times 2)$ -O/Cu], as illustrated in the inset of Fig. 3(a). This assignment is further substantiated by our DFT simulations (see the Supplemental Material, Fig. S4 [31]), and also by the analysis of the electronic density of states in the following discussion.

Interestingly, those stripes in Fig. 3(a) appear to originate from a fully reconstructed “core” region and radiate out to form a sunflowerlike pattern (see more examples in the Supplemental Material, Fig. S5 [31]). Moreover, the FRR is usually located near the Cu surface steps, and the step appears more reactive for oxygen absorption during exposure to the air. This is consistent with previous reports that steps can bind adsorbates more strongly than terrace sites on metal surfaces [51]. In addition, we find that some oxygen atoms are still mobile at room temperature by tracing the locations of oxygen vacancies in Fig. 3(c) (marked by dashed circles). These defects can diffuse [Fig. 3(d)] and even disappear from the field of view [Fig. 3(e)] during STM scanning at room temperature. Our DFT calculations show a diffusion barrier of 0.74 eV for an oxygen atom traveling from one to the neighboring hollow site via a bridge site, similar to a previous report [52]. By employing an attempt frequency of $\sim 10^{13}$ Hz [53] and a potential barrier of 0.74 eV, the hopping rate of oxygen is estimated as ~ 3.3 s⁻¹ at room temperature. Thus the oxygen diffusion is observable in the STM image at room temperature as shown in Figs. 3(c)–3(e) and by Yagyu *et al.* [54]. Note, the bright spots in STM images are believed to be

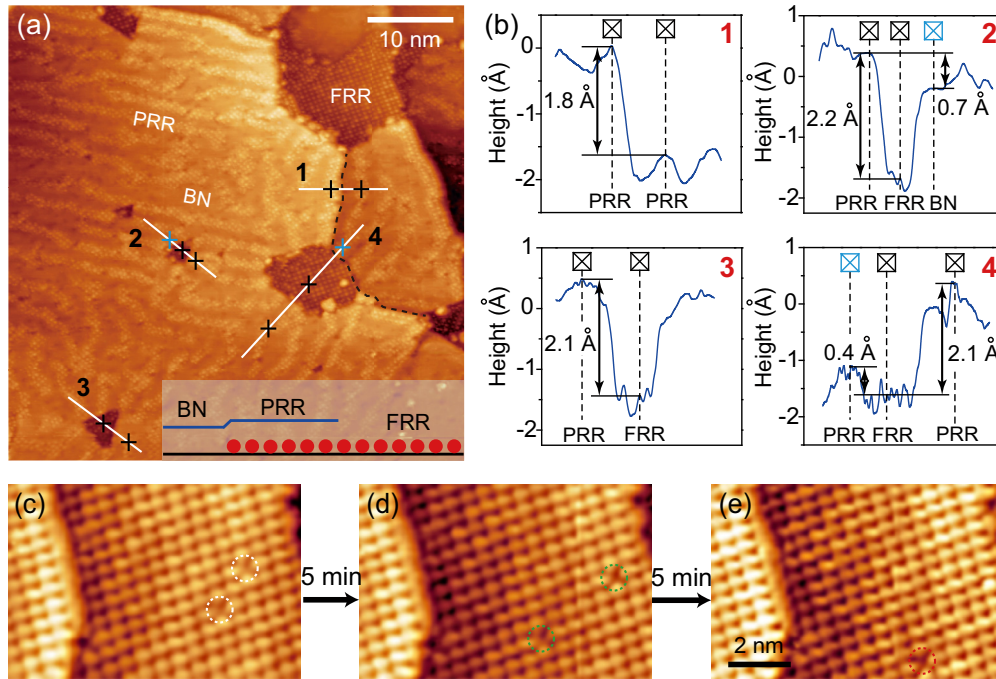


FIG. 3. Oxygen diffusion in monolayer h -BN on Cu(100) after 600 °C annealing (1 h, following overnight degassing at 430 °C after 20 h air exposure; sample B). (a) STM image showing a checkerboardlike pattern formed by fully reconstructed regions (FRRs) and quasi-1D stripes at the partially reconstructed regions (PRRs) (−1 V, 100 pA). Inset: Schematic cross-sectional view of h -BN, partially and fully reconstructed regions on Cu. Red dots, adsorbed oxygen atoms. (b) STM height profiles along white lines marked in (a). Line 1: PRRs across a Cu substrate atomic step (marked with dashed black line). Lines 2 and 3: FRRs surrounded by PRRs without Cu steps. Line 4: An FRR surrounded by PRRs coinciding with a Cu step. (c)–(e) STM images of the same area with 5 min time intervals showing the diffusion of oxygen vacancies in the $p(2 \times 2)$ -O superstructure. Dashed circles marked the positions of the vacancies (+1V, 60 pA).

associated with oxygen due to their protrusion above the Cu lattice and enhanced electronic density of states [47].

DFT calculations were performed to understand the reconstruction process and specifically the formation mechanism of the novel $p(2 \times 2)$ oxygen superstructures in the van der Waals heterostructure (see Sec. II and the Supplemental Material, Fig. S4 [31] for calculation details). Figure 4(a) shows our atomistic modeling of h -BN monolayer on Cu(100), where the supercell results in BN wrinkles with a period that matches to the experimentally observed moiré patterns in Fig. 4(b) (black dashed lines). A slight compressive strain is applied to h -BN because of the lattice mismatch between Cu(100) and BN in our supercell configuration, which induces the vertical wrinkles in the h -BN along the armchair direction with a period of 1.28 nm ($5a_{\text{Cu}} \sim 6a_{\text{BN}}\sin 60^\circ$) [30]. The period is in good agreement with the experimental value of 1.26 nm (see black lines in Fig. 4(b) and also the Supplemental Material, Fig. S6 [31]). Figure 4(c) displays a theoretically identified stable $p(2 \times 2)$ -O superstructure with a coverage $\Theta = 0.4$, where the period of the stripes is twice the period of the moiré patterns in the pristine BN/Cu without any oxygen; the period of $10a_{\text{Cu}}$ ($= 2.56$ nm) agrees well with the experimental value of 2.52 nm [see white dashed lines in Fig. 4(b)]. We then compared the $p(2 \times 2)$ and $(2\sqrt{2} \times \sqrt{2})R45^\circ$ oxygen superstructures with and without the h -BN overlayer. Superstructures with different effective oxygen coverage are also considered (see the Supplemental Material, Fig. S6 [31]).

We evaluate the relative structural stabilities of oxygen reconstructed Cu(100) surfaces in comparison to the bare surfaces. Then we construct a phase diagram that identifies stable phases between the pristine systems without any oxygen adsorption and the stripelike $p(2 \times 2)$ and $(2\sqrt{2} \times \sqrt{2})R45^\circ$ oxygen superstructures depending on the oxygen chemical potential with respect to that in Cu₂O bulk, $\Delta\mu_{\text{O}}$, and the oxygen superstructure coverage Θ . Figures 4(d) and 4(e) present the phase diagrams with and without h -BN, respectively. In both cases, the area of the stable region of $p(2 \times 2)$ becomes larger as the coverage decreases, while the trend is opposite for that of $(2\sqrt{2} \times \sqrt{2})R45^\circ$. This indicates that for a given (partial) coverage the $p(2 \times 2)$ -O superstructure of a separated stripe pattern is more accessible than the aggregated phase in a wide range of chemical potentials. With the partial coverage, the presence of the moiré patterns generates confined channels along the zigzag direction of h -BN, providing an efficient pathway for oxygen intercalation and diffusion and thus helping paired $p(2 \times 2)$ oxygen to form PRR. Experimentally, the thermal-driven diffusion of oxygen can also induce the fluctuation of the width and direction of the PRRs (Fig. 3). Moreover, if we compare the $\Delta\mu_{\text{O}}$ range for the stable $p(2 \times 2)$ phase at $\Theta = 1$, the stable region without h -BN is found much larger than that with h -BN. Such a stability reduction of h -BN/ $p(2 \times 2)$ -O/Cu compared to the case without h -BN can explain why oxygen-mediated etching of h -BN prefers to occur in the FRR. Although our DFT calculations shed light on the formation of the $p(2 \times 2)$ -O superstructures in

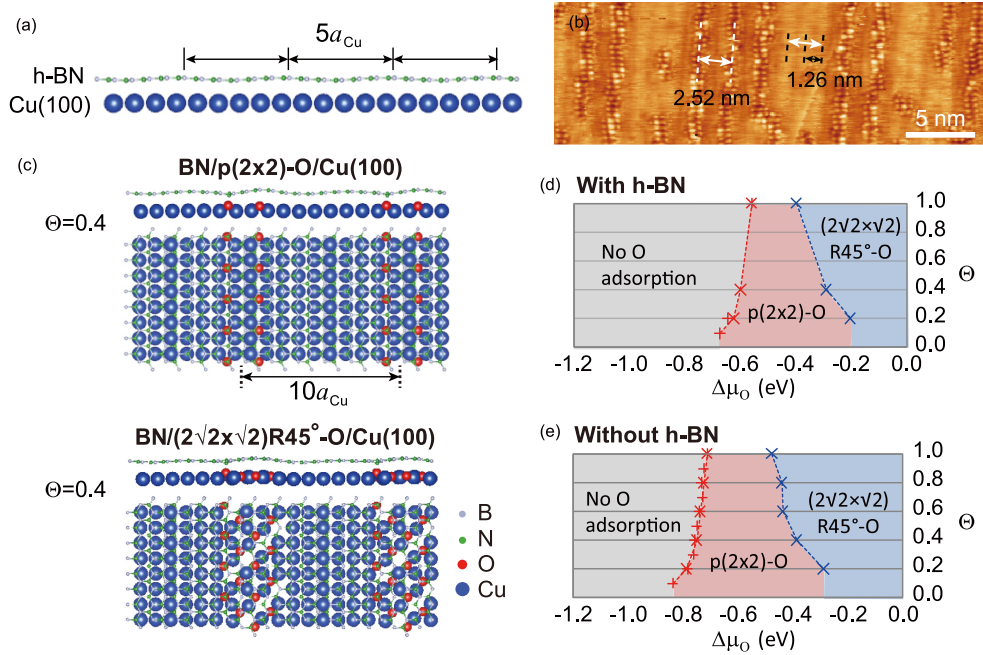


FIG. 4. Phase diagrams of O superstructures in h -BN/Cu(100). (a) The structure model of the h -BN/Cu(100) interface used in the DFT calculations (side view). (b) STM image showing $p(2 \times 2)$ -O stripes intercalated at the h -BN/Cu(100) interface (+0.5 V, 100 pA). Black and white dashed lines marked the moiré patterns and the $p(2 \times 2)$ -O stripes, respectively. (c) Calculated stable structures of $p(2 \times 2)$ -O (upper panel) and $(2\sqrt{2} \times \sqrt{2})R45^\circ$ -O (lower panel) in h -BN/Cu(100) with an effective oxygen superstructure coverage $\Theta = 0.4$. Both side view and top view structures are presented. (d) and (e) Calculated phase diagrams of oxygen superstructures (d) with and (e) without h -BN overlayer. Here only oxygen superstructures with striped patterns are considered. Regions marked with different colors correspond to the stable phases, in consideration of oxygen chemical potential ($\Delta\mu_O$) at different oxygen superstructure coverages with respect to that in Cu_2O bulk.

the presence of h -BN, which is also consistent with previous results [47], the specific mechanism necessitates further study.

To understand the effect of the O superstructure on the h -BN overlayer, we examined the density of states (DOS) of different regions in sample B (20 h air exposure, 1 h 600 °C annealing) by scanning tunneling spectroscopy (STS) measurements. Figure 5(a) shows clearly that band gaps exist in the $p(2 \times 2)$ -O intercalated region [PRR, i.e., $\text{BN}/p(2 \times 2)$ -O/Cu] and pristine h -BN region. The apparent band gap of the h -BN monolayer on Cu is ~ 3.6 eV, consistent with previous measurements [32]. With the intercalated $p(2 \times 2)$ -O superstructure, the PRR shows a larger band gap of ~ 5.3 eV, which is close to the band gaps in h -BN crystals [23]. The green curve acquired from the fully reconstructed region [FRR, i.e., $p(2 \times 2)$ -O/Cu] shows a metallic feature [47]. The tunneling dI/dV curves in the vicinity of the Fermi energy (indicative of in-gap states) are shown in Fig. 5(b) with a smaller bias range. A local tunneling conductance maximum is obtained at about -0.25 eV (marked with an arrow) in the h -BN region but not in the $p(2 \times 2)$ -O containing regions. The -0.25 eV band is associated with the Cu(100) surface [32,55]. The Cu surface is passivated by the $p(2 \times 2)$ -O superstructure in reconstructed regions, which effectively decouples the h -BN from the underlying Cu substrate, resulting in the intrinsic band gap in the h -BN overlay. As a result, atomically resolved STM images are obtained on h -BN/Cu but not on h -BN/ $p(2 \times 2)$ -O/Cu.

Both experimental tunneling spectroscopy data and simulated DOS show a metallic behavior of the $p(2 \times 2)$ -O. As DFT

calculations can accurately determine the energies of occupied states but underestimate the energies of the unoccupied states [56], in Fig. 5(c) we examine the valence band maximum (VBM) by setting the expected BN VBM as zero energy. As illustrated in Figs. 5(a) and 5(c) with dashed boxes, both measured and calculated energies of the VBM show a downward shift after the $p(2 \times 2)$ -O intercalation, which leads to an enlarged band gap. Based on the calculations, we find that without the intercalated $p(2 \times 2)$ -O, the Cu 3d bands show up in the band gap of BN and extend to about 1.0 eV above the BN VBM. The intercalation of $p(2 \times 2)$ -O suppresses the contribution of Cu states, while the contribution of O 2p bands to the BN band gap is up to 0.7 eV above the BN VBM. The Cu-3d and O-2p band tail features obtained in DFT calculations are very similar to those obtained in STS measurements in the dashed box regions.

To gain further insight into the effect of oxygen superstructures on the stability of h -BN, we performed STM investigations on the structural and electronic properties of h -BN islands in sample A. Figures 6(a) and 6(b) show the monolayer h -BN nanoislands surrounded by the oxygen superstructures, indicating a strong etching effect of the monolayer h -BN. Three regions with clear boundaries are observed, especially for the positive bias, corresponding to the $p(2 \times 2)$ -O, the h -BN, and a transition region labeled as etching front, respectively. The etching front is parallel to the quasi-1D $p(2 \times 2)$ -O superstructure. The STM image of the transition region is bias dependent, opaque in negative

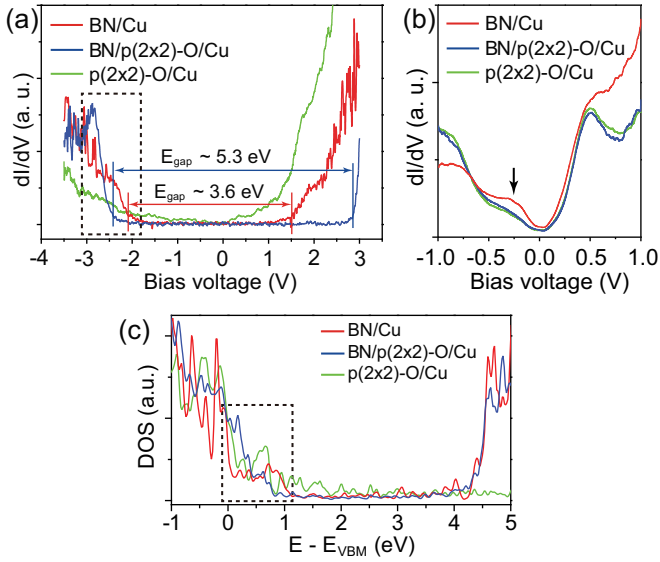


FIG. 5. Electronically decoupling between the monolayer h -BN and Cu(100) by the intercalated $p(2 \times 2)$ -O superstructure. (a) dI/dV curves (-3.5 V, 100 pA) showing band gaps of about 5.3 and 3.6 eV for h -BN with (blue) and without (red) the intercalated $p(2 \times 2)$ -O superstructure, respectively. The dI/dV curve acquired from $p(2 \times 2)$ -O on exposed Cu is also shown (green). (b) Small bias range dI/dV curves (-1 V, 100 pA) near the Fermi energy for the three regions. The black arrow marks the feature associated with the Cu(100) surface. (c) Simulated densities of states (DOS) of the $p(2 \times 2)$ -O (green) and BN with (blue) and without (red) intercalated $p(2 \times 2)$ -O on Cu(100). The energy is set against the expected valence band maximum (VBM) of BN. Dashed boxes marked the features near the VBM of BN in (a) experiment and (c) theory.

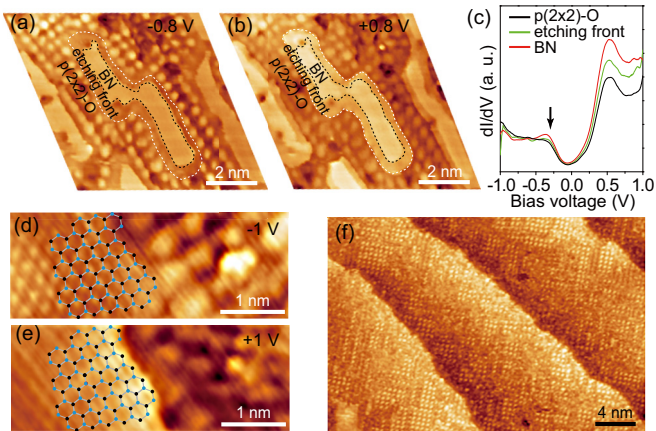


FIG. 6. Oxygen-mediated catalytic disintegration of h -BN on Cu(100). (a) and (b) Simultaneously acquired dual bias (± 0.8 V) topographic STM images, showing h -BN nanoislands separated by the $p(2 \times 2)$ -O superstructure after annealing at 600 °C for 4 h (sample A). Three regions are marked with dashed lines to indicate regions of reconstructed, etching front, and h -BN, respectively. (c) dI/dV spectra of the three regions (-1 V, 100 pA). The arrow marks the feature of the Cu(100) surface. (d) and (e) STM images acquired at -1 and $+1$ V, respectively, showing the atomic resolution and zigzag edges of the monolayer h -BN (blue: N; black: B). (f) STM image showing the complete removal of h -BN on Cu(100) after annealing at 600 °C for 12 h ($+0.6$ V, 400 pA).

bias and transparent in positive bias (additional examples of the three different regions are shown in the Supplemental Material, Fig. S7 [31]). Here we find that even in quasi-1D superstructure regions the h -BN overlayer has been etched in sample A, different from the case of sample B (Fig. 3), although they both appear as quasi-1D stripes. This difference may be ascribed to the longer annealing time of sample A (4 h) than sample B (1 h), which promotes the etching of the h -BN. In sample A, the h -BN overlayers have also been etched in both the 2D and quasi-1D $p(2 \times 2)$ -O superstructure regions (shown in Fig. 1), which gives an area statistic value consistent with the XPS results in Fig. 2. STS curves acquired at the three regions are shown in Fig. 6(c), similar to those shown in Fig. 5(b). In the $p(2 \times 2)$ -O region, the Cu surface is passivated by the superstructures. In the h -BN region, the Cu surface peak (marked with an arrow) is obviously stronger than the other two regions. In the transition region, oxygen starts to intercalate in h -BN/Cu, as evident by the oxygen-induced superstructure discernable under the h -BN in Figs. 6(a) and 6(b). These observations indicate that the h -BN etching proceeds via the intercalation of oxygen atoms. The edge structure of an h -BN nanoisland is shown in Figs. 6(d) and 6(e) at negative and positive biases, respectively. As further shown in the Supplemental Material, Fig. S8 [31], the edges are zigzag, similar to those formed by high-energy electron irradiation etching [57–59]. After annealing the sample at 600 °C for 12 h, almost all h -BN is removed and the copper surface is predominantly covered by $p(2 \times 2)$ -O superstructure, as shown in Fig. 6(f). The superstructure is displayed as small patches, usually with two or three paired oxygen atoms. This result is also consistent with DFT results in Fig. 4, where a surface with partial oxygen coverage is shown to be more stable than a full covered surface on Cu(100). However, when surrounded by monolayer h -BN, the FRRs show a very different picture that the $p(2 \times 2)$ -O superstructures can be as large as tens of nanometers (Figs. 1 and 3). The etching process also leads to the loss of oxygen [60], however additional oxygen beneath the surface of copper, such as soluble oxygen [61] and copper oxides [62,63], may diffuse to the surface during thermal annealing process and contribute to the observation in Fig. 6 where the remaining oxygen atoms are still visible on the exposed Cu surfaces.

Altogether, our observations suggest the following atomistic picture of oxygen adsorption on h -BN/Cu(100). During the air exposure, oxygen molecules intercalate under h -BN on Cu through defects and grain boundaries, and are trapped preferentially at step edges of Cu, where copper oxide (Cu_2O) can easily form [17]. At elevated temperatures around 600 °C, the dissociated oxygen atoms from the copper oxide form ordered $p(2 \times 2)$ -O superstructures on the copper surface due to repulsions between the on-surface oxygen atoms [64]. Oxygen-mediated etching of h -BN may initiate at defects and Cu steps, resulting in FRRs (oxygen superstructures without an h -BN overlayer). Oxygen atoms diffuse from the fully reconstructed regions to intercalate the h -BN preferably along the pre-existing moiré patterns in the interface, forming the quasi-1D stripes of paired oxygen. The oxygen intercalation slightly increases the distance between h -BN and Cu substrate, suppresses the contribution of Cu surface in the tunneling conductance, and further decouples the h -BN from the Cu.

The monolayer *h*-BN can be effectively etched by intercalated oxygen when annealed at 600 °C in UHV. The confined oxygen will etch the nearby *h*-BN, first forming a sunflowerlike pattern with fully reconstructed regions surrounded by oxygen intercalated *h*-BN stripes, and then completely removing all the *h*-BN and leaving a reconstructed Cu surface. The FRRs exhibit large-area superstructures when surrounded by PRRs (Figs. 1(a) and 3(a) and the Supplemental Material [31]) while the Cu surface after complete *h*-BN removal exhibits small $p(2 \times 2)$ patches of several O atoms. The catalytic oxygen-mediated etching of the *h*-BN is similar to recent works [15–17]. Namely, the etching process generates N₂ and volatile boron oxide [17], thus it does not result in additional signal from N1s or B1s in *ex situ* XPS shown in Figs. 2(b) and 2(c). Unlike the reports that monolayer *h*-BN transferred to a SiO₂/Si substrate starts the disintegration by forming oxygen chains and dissociation of the B–O–N bonds on top of BN [22,27,28], our results support a different picture of the oxygen diffusion and etching of the *h*-BN covered metals [17]. The *h*-BN monolayer on Cu(100) surface cannot prevent the oxidation of the metal substrate at 600 °C because of the catalytic oxygen-mediated etching effect of the *h*-BN. Recently, few-layer and multilayer *h*-BN have been recommended as high-temperature oxidation-resistant coatings on metals including Cu and Ni [26]. In this case, the additional layers of *h*-BN may have provided an effective barrier for oxygen intercalation; otherwise, the layers in contact with the catalytic metal would have been etched by the intercalated oxygen. Exposure to air is often unavoidable in process integration and 2D heterostructures [65]; especially, BN nanosheets have a strong tendency to adsorb organic contaminations from both atmosphere and lithographic processes [66]. *h*-BN layers have been widely used as a capping layer to isolate 2D materials from air in nanotransistors [25,67], where the etching effect of the intercalated oxygen between the metal electrodes and *h*-BN should be considered, especially when high temperature annealing is involved. It is thus critically important to understand and control the effect of oxygen intercalation and oxygen-mediated defect formation in order to make use of the unique electronic, mechanic, chemical, and temperature stability of *h*-BN.

IV. CONCLUSIONS

In summary, Cu(100) $p(2 \times 2)$ oxygen superstructures are revealed in monolayer *h*-BN/Cu after exposure to air and subsequent high temperature annealing in vacuum. Both 2D and quasi-1D patterns are observed in association with the oxygen absorption on Cu. The 2D pattern of $p(2 \times 2)$ -O is found near surface steps of the Cu, while the quasi-1D pattern is formed by oxygen intercalation under *h*-BN on Cu(100) where the confinement of interface in the moiré patterns plays an important role in the formation of the superstructure. The oxygen intercalation starts from the 2D $p(2 \times 2)$ -O regions and preferentially follows the confined space of the pre-existing moiré patterns of *h*-BN/Cu(100) to form stable quasi-1D $p(2 \times 2)$ -O stripes. The existence of the $p(2 \times 2)$ -O superstructures can passivate the Cu surface and decouple the monolayer *h*-BN from the metal. After prolonged air exposure and thermal annealing at 600 °C, large area *h*-BN monolayers are etched into nanoislands with zigzag edges and can even be removed completely. An oxygen-mediated catalytic etching process is believed to be responsible for the disintegration of the *h*-BN monolayer. The etching of the *h*-BN overlays follows the oxygen diffusion process and leaves the *h*-BN nanoislands with zigzag edges. Our results directly show the interplay between the novel $p(2 \times 2)$ -O superstructures and the monolayer *h*-BN on Cu(100), and can provide a deeper understanding of the formation of defects in and the stability of *h*-BN on metals.

ACKNOWLEDGMENTS

This research was conducted at the Center for Nanophase Materials Sciences, which is a DOE Office of Science User Facility. STM measurements by C.M. were supported by the Laboratory Directed Research and Development Program of Oak Ridge National Laboratory, managed by UT-Battelle, LLC, for the U. S. DOE. The work at UTK was supported by NSF (Grant No. ECCS-1231808) and DARPA (Grant No. HR0011-13-2-0016). Computational research used resources of the National Energy Research Scientific Computing Center, a DOE Office of Science User Facility under Contract No. DE-AC02-05CH11231.

-
- [1] A. Ohtomo and H. Y. Hwang, *Nature (London)* **427**, 423 (2004).
 - [2] M. Sing, G. Berner, K. Goß, A. Müller, A. Ruff, A. Wetscherek, S. Thiel, J. Mannhart, S. A. Pauli, C. W. Schneider, P. R. Willmott, M. Gorgoi, F. Schäfers, and R. Claessen, *Phys. Rev. Lett.* **102**, 176805 (2009).
 - [3] Q. Fu, W.-X. Li, Y. Yao, H. Liu, H.-Y. Su, D. Ma, X.-K. Gu, L. Chen, Z. Wang, H. Zhang, B. Wang, and X. Bao, *Science* **328**, 1141 (2010).
 - [4] V. V. Volkov, D. J. Palmer, and R. Righini, *Phys. Rev. Lett.* **99**, 078302 (2007).
 - [5] D. E. Moilanen, N. E. Levinger, D. B. Spry, and M. D. Fayer, *J. Am. Chem. Soc.* **129**, 14311 (2007).
 - [6] Y. Zhang, X. Weng, H. Li, M. Wei, J. Xiao, Z. Liu, M. Chen, Q. Fu, and X. Bao, *Nano Lett.* **15**, 3616 (2015).
 - [7] H. Cun, M. Iannuzzi, A. Hemmi, S. Roth, J. Osterwalder, and T. Greber, *Nano Lett.* **13**, 2098 (2013).
 - [8] A. B. Preobrajenski, M. L. Ng, N. A. Vinogradov, A. S. Vinogradov, E. Lundgren, A. Mikkelsen, and N. Mårtensson, *Nano Lett.* **9**, 2780 (2009).
 - [9] Y. Zhang, Y. Zhang, D. Ma, Q. Ji, W. Fang, J. Shi, T. Gao, M. Liu, Y. Gao, Y. Chen, L. Xu, and Z. Liu, *Nano Res.* **6**, 887 (2013).
 - [10] E. Grånäs, J. Knudsen, U. A. Schröder, T. Gerber, C. Busse, M. A. Arman, K. Schulte, J. N. Andersen, and T. Michely, *ACS Nano* **6**, 9951 (2012).
 - [11] X. Li, W. Cai, J. An, S. Kim, J. Nah, D. Yang, R. Piner, A. Velamakanni, I. Jung, E. Tutuc, S. K. Banerjee, L. Colombo, and R. S. Ruoff, *Science* **324**, 1312 (2009).
 - [12] S. Joshi, D. Eciya, R. Koitz, M. Iannuzzi, A. P. Seitsonen, J. Hutter, H. Sachdev, S. Vijayaraghavan, F. Bischoff, K. Seufert, J. V. Barth, and W. Auwärter, *Nano Lett.* **12**, 5821 (2012).

- [13] M. Corso, W. Auwärter, M. Muntwiler, A. Tamai, T. Greber, and J. Osterwalder, *Science* **303**, 217 (2004).
- [14] Y. Yang, Q. Fu, M. Wei, H. Bluhm, and X. Bao, *Nano Res.* **8**, 227 (2015).
- [15] K. A. Simonov, N. A. Vinogradov, M. L. Ng, A. S. Vinogradov, N. Mårtensson, and A. B. Preobrajenski, *Surf. Sci.* **606**, 564 (2012).
- [16] A. Goriachko, A. A. Zakharov, and H. Over, *J. Phys. Chem. C* **112**, 10423 (2008).
- [17] P. R. Kidambi, R. Blume, J. Kling, J. B. Wagner, C. Baetz, R. S. Weatherup, R. Schloegl, B. C. Bayer, and S. Hofmann, *Chem. Mater.* **26**, 6380 (2014).
- [18] G. J. Slotman and A. Fasolino, *J. Phys.: Condens. Matter* **25**, 045009 (2013).
- [19] N. Kostoglou, K. Polychronopoulou, and C. Rebholz, *Vacuum* **112**, 42 (2015).
- [20] L. Song, L. Ci, H. Lu, P. B. Sorokin, C. Jin, J. Ni, A. G. Kvashnin, D. G. Kvashnin, J. Lou, B. I. Yakobson, and P. M. Ajayan, *Nano Lett.* **10**, 3209 (2010).
- [21] Y. Chen, J. Zou, S. J. Campbell, and G. Le Caer, *Appl. Phys. Lett.* **84**, 2430 (2004).
- [22] L. H. Li, J. Cervenka, K. Watanabe, T. Taniguchi, and Y. Chen, *ACS Nano* **8**, 1457 (2014).
- [23] Y. Kubota, K. Watanabe, O. Tsuda, and T. Taniguchi, *Science* **317**, 932 (2007).
- [24] C. R. Dean, A. F. Young, I. Meric, C. Lee, L. Wang, S. Sorgenfrei, K. Watanabe, T. Taniguchi, P. Kim, K. L. Shepard, and J. Hone, *Nat. Nanotech.* **5**, 722 (2010).
- [25] A. K. Geim and I. V. Grigorieva, *Nature (London)* **499**, 419 (2013).
- [26] Z. Liu, Y. Gong, W. Zhou, L. Ma, J. Yu, J. C. Idrobo, J. Jung, A. H. MacDonald, R. Vajtai, J. Lou, and P. M. Ajayan, *Nat. Commun.* **4**, 2541 (2013).
- [27] M. S. Si and D. S. Xue, *J. Phys. Chem. Solid* **71**, 1221 (2010).
- [28] Y. Zhao, X. Wu, J. Yang, and X. C. Zeng, *Phys. Chem. Chem. Phys.* **14**, 5545 (2012).
- [29] L. Liu, J. Park, D. A. Siegel, K. F. McCarty, K. W. Clark, W. Deng, L. Basile, J. C. Idrobo, A.-P. Li, and G. Gu, *Science* **343**, 163 (2014).
- [30] L. Liu, D. A. Siegel, W. Chen, P. Liu, J. Guo, G. Duscher, C. Zhao, H. Wang, W. Wang, X. Bai, K. F. McCarty, Z. Zhang, and G. Gu, *Proc. Natl. Acad. Sci. USA* **111**, 16670 (2014).
- [31] See Supplemental Material at <http://link.aps.org/supplemental/10.1103/PhysRevB.94.064106> for information of the SEM images, XPS spectra, computation details, and more STM images and STS curves.
- [32] J. Park, J. Lee, L. Liu, K. W. Clark, C. Durand, C. Park, B. G. Sumpter, A. P. Baddorf, A. Mohsin, M. Yoon, G. Gu, and A.-P. Li, *Nat. Commun.* **5**, 5403 (2014).
- [33] J. Cho, L. Gao, J. Tian, H. Cao, W. Wu, Q. Yu, E. N. Yitamben, B. Fisher, J. R. Guest, Y. P. Chen, and N. P. Guisinger, *ACS Nano* **5**, 3607 (2011).
- [34] G. Kresse and J. Furthmüller, *Comput. Mater. Sci.* **6**, 15 (1996).
- [35] G. Kresse and J. Furthmüller, *Phys. Rev. B* **54**, 11169 (1996).
- [36] P. E. Blöchl, *Phys. Rev. B* **50**, 17953 (1994).
- [37] G. Kresse and D. Joubert, *Phys. Rev. B* **59**, 1758 (1999).
- [38] J. P. Perdew, K. Burke, and M. Ernzerhof, *Phys. Rev. Lett.* **77**, 3865 (1996).
- [39] S. Grimme, *J. Comp. Chem.* **27**, 1787 (2006).
- [40] S. Grimme, J. Antony, S. Ehrlich, and H. Krieg, *J. Chem. Phys.* **132**, 154104 (2010).
- [41] J. Lu, P. S. E. Yeo, Y. Zheng, H. Xu, C. K. Gan, M. B. Sullivan, A. H. Castro Neto, and K. P. Loh, *J. Am. Chem. Soc.* **135**, 2368 (2013).
- [42] Y. Gao, Y. Zhang, P. Chen, Y. Li, M. Liu, T. Gao, D. Ma, Y. Chen, Z. Cheng, X. Qiu, W. Duan, and Z. Liu, *Nano Lett.* **13**, 3439 (2013).
- [43] W. Auwärter, H. U. Suter, H. Sachdev, and T. Greber, *Chem. Mater.* **16**, 343 (2004).
- [44] U. Döbler, K. Baberschke, J. Stöhr, and D. A. Outka, *Phys. Rev. B* **31**, 2532 (1985).
- [45] E. Vlieg, I. K. Robinson, and R. McGrath, *Phys. Rev. B* **41**, 7896 (1990).
- [46] J. Moulder, W. Stickle, P. Sobol, and K. Bomben, *Handbook of X Ray Photoelectron Spectroscopy (P/N 624755)* (Physical Electronics Division, Perkin-Elmer, Waltham, MA, 1992).
- [47] X. Duan, O. Warschkow, A. Soon, B. Delley, and C. Stampfl, *Phys. Rev. B* **81**, 075430 (2010).
- [48] J. A. Barker and I. P. Batra, *Phys. Rev. B* **27**, 3138 (1983).
- [49] M. J. Harrison, D. P. Woodruff, J. Robinson, D. Sander, W. Pan, and J. Kirschner, *Phys. Rev. B* **74**, 165402 (2006).
- [50] F. Jensen, F. Besenbacher, E. Laegsgaard, and I. Stensgaard, *Phys. Rev. B* **42**, 9206 (1990).
- [51] N. Bonini, A. Kokalj, A. Dal Corso, S. de Gironcoli, and S. Baroni, *Phys. Rev. B* **69**, 195401 (2004).
- [52] M. Alatalo, S. Jaatinen, P. Salo, and K. Laasonen, *Phys. Rev. B* **70**, 245417 (2004).
- [53] M. Wuttig, R. Franchy, and H. Ibach, *Surf. Sci.* **213**, 103 (1989).
- [54] K. Yagyu, X. Liu, Y. Yoshimoto, K. Nakatsuji, and F. Komori, *J. Phys. Chem. C* **113**, 5541 (2009).
- [55] J. Tian, H. Cao, W. Wu, Q. Yu, N. P. Guisinger, and Y. P. Chen, *Nano Lett.* **12**, 3893 (2012).
- [56] D. S. Sholl and J. A. Steckel, *Density Functional Theory: A Practical Introduction* (John Wiley and Sons, Canada, 2011).
- [57] C. Jin, F. Lin, K. Suenaga, and S. Iijima, *Phys. Rev. Lett.* **102**, 195505 (2009).
- [58] N. Alem, R. Erni, C. Kisielowski, M. D. Rossell, W. Gannett, and A. Zettl, *Phys. Rev. B* **80**, 155425 (2009).
- [59] J. Kotakoski, C. H. Jin, O. Lehtinen, K. Suenaga, and A. V. Krashenninnikov, *Phys. Rev. B* **82**, 113404 (2010).
- [60] S. Yu. Rybakov, V. M. Sharapov, and L. E. Gavrilov, *J. Phys. IV France* **5**, C5-921 (1995).
- [61] Edited by J. R. Davis, *ASM Specialty Handbook: Copper and Copper Alloys* (ASM International, Materials Park, OH, 2001).
- [62] F. W. Young, J. V. Cathcart, and A. T. Gwathmey, *Acta Metall.* **4**, 145 (1956).
- [63] J. C. Yang, B. Kolasa, J. M. Gibson, and M. Yeadon, *Appl. Phys. Lett.* **73**, 2841 (1998).
- [64] S. Jaatinen, J. Blomqvist, P. Salo, A. Puisto, M. Alatalo, M. Hirsimäki, M. Ahonen, and M. Valden, *Phys. Rev. B* **75**, 075402 (2007).
- [65] Q. Li, M. Liu, Y. Zhang, and Z. Liu, *Small* **12**, 32 (2016).
- [66] A. G. F. Garcia, M. Neumann, F. Amet, J. R. Williams, K. Watanabe, T. Taniguchi, and D. Goldhaber-Gordon, *Nano Lett.* **12**, 4449 (2012).
- [67] H. Liu, A. T. Neal, Z. Zhu, Z. Luo, X. Xu, D. Tománek, and P. D. Ye, *ACS Nano* **8**, 4033 (2014).